Journal of Power Sources 262 (2014) 501–513

Contents lists available at ScienceDirect

Journal of Power Sources

journal homepage: www.elsevier.com/locate/jpowsour

Quantification of contributions to the cell overpotential during galvanostatic discharge of a lithium-ion cell

Rajeswari Chandrasekaran

Research and Advanced Engineering, Ford Motor Company, Dearborn, MI 48124, USA

HIGHLIGHTS

- Validated the lithium-ion cell sandwich model with experimental data.
- Quantified and analyzed the overpotential contributions at high discharge rates.
- Magnitude and contributions of overpotentials vary with discharge rate and time.

ARTICLE INFO

Article history:
Received 21 February 2014
Received in revised form
24 March 2014
Accepted 25 March 2014
Available online 2 April 2014

Keywords:
Lithium-ion
Modeling
Automotive
Electric vehicles
Batteries
Performance

ABSTRACT

Isothermal, physics-based cell sandwich model has been validated with experimental galvanostatic discharge data at various current densities for advanced lithium-ion cells. The overpotential is higher at higher current densities and mostly increases with discharge at any given rate. The various contributions to cell overpotential during galvanostatic discharge at 5C and 3C constant-current densities are quantified in detail and analyzed. This work will aid in research and development efforts to mitigate these limitations for better cell performance in potential advanced electric vehicle applications.

1. Introduction

Lithium-ion cells designed for traction in advanced electric vehicles should have high gravimetric and volumetric energy and power densities so that the battery pack weigh less and occupy less space while delivering the desired range and acceleration. This is possible if capacity and overpotential losses are minimized. Therefore quantification of capacity [1–3] and voltage [4,5] losses are essential for gaining insight into necessary mitigation strategies. Modeling enables detailed spatial–temporal analyses of responses of interest at a fraction of cost and time as compared to experiments.

In this work, isothermal, physics-based cell sandwich model predictions are validated with experimental galvanostatic discharge data at various current densities (rates) for advanced lithium-ion cells. The contributions to cell overpotential during galvanostatic discharge at higher rates are quantified and analyzed in detail. This aids in research and development efforts both in-house and among our collaborators to mitigate these limitations for better cell performance in potential advanced electric vehicle applications.

2. Modeling

The galvanostatic discharge of Li_xC_6/liquid electrolyte/$Li_y(Ni_aCo_bMn_c)O_2$ [6], i.e. dual lithium-ion insertion cell sandwich is modeled using macro-homogenous approach and concentrated solution theory [7,8]. The liquid electrolyte is $LiPF_6$ in EC:EMC:DMC in the ratio 3:4:3 with additives. The underlying theories and equations have been discussed extensively in the past [7,8] and are not repeated here. The open-circuit potential vs. composition curves for the electrodes and the experimental discharge curves are taken from prior work [6]. The experimental galvanostatic discharge curves (cell capacity vs. voltage plots) [6] were obtained at 25 °C using an 18650 surrogate cell format with a designed discharge capacity of 230 mAh (21.30 A m^{-2} is the ideal 1C-rate). Other properties and parameters that are used in this work are

E-mail address: rchand35@ford.com.

http://dx.doi.org/10.1016/j.jpowsour.2014.03.124
0378-7753/

provided in Table 1 and Appendix A and more details are available in the previous work [6].

The simulations of the coupled, transient, partial differential equations at all galvanostatic discharge rates are carried out at 298 K, to the cut-off potential of 2.8 V (as in experiments) using COMSOL multiphysics finite element software (version 4.3). Time dependent, non-linear solver is used. Backward differentiation formula is used for time stepping.

Model coupling operators such as 'integration' and 'average' were defined in domains of interest in COMSOL and were called upon during post-processing to obtain the various overpotentials using corresponding expressions in the cell sandwich model.

3. Results and discussions

The comparison between experimental data and model predictions are provided in Fig. 1. It should be noted that only a portion of the experimental data points are shown as symbols for purposes of clarity. The cell capacity obtained during discharge by coulomb counting indicates the depth (or state or degree) of discharge or utilization of the cell until that time step.

3.1. Contributions to cell overpotential from simulations

Cell overpotential is the difference between the thermodynamic open-circuit potential of the cell and the simulated cell voltage. Fig. 2 gives the cell overpotential at all discharge rates from simulation results and as expected, the overpotential is higher at higher rates of discharge. Up to 1C, the overpotential has remained almost constant throughout discharge at a given rate and increases only slightly towards the end at C/2 and C-rate current densities.

Table 1
Model input parameters.

Parameter description	Value
Constant-current density at 1C discharge rate	21.3 A m^{-2}
Radius of the secondary particle of the negative electrode active material	6.35 μm
C-rates at which the cell is discharged	0.2; 0.5; 1; 3; 5
Radius of the secondary particle of the positive electrode active material	5.15 μm
Transference number	0.363
Salt diffusion coefficient (for C/5–3C rate)	7×10^{-11} m^2 s^{-1}
Salt diffusion coefficient (for 5C rate)	9.8×10^{-11} m^2 s^{-1}
Active material volume fraction in the positive electrode	0.62
Electrolyte volume fraction in the positive electrode	0.29
Bulk solid matrix electronic conductivity (positive)	0.5121 S m^{-1}
Bulk solid matrix electronic conductivity (negative)	4.3317 S m^{-1}
Initial electrolyte concentration	1300 mol m^{-3}
Active material volume fraction in the negative	0.65
Electrolyte (pore) volume fraction in the negative	0.33
Maximum solid phase lithium concentration (negative)	30,813 mol m^{-3}
Maximum solid phase lithium concentration (positive)	51,000 mol m^{-3}
Initial solid phase lithium concentration (negative)	20,469 mol m^{-3}
Initial solid phase lithium concentration (positive)	13,872 mol m^{-3}
Kinetic rate constant (negative)	1×10^{-11} m s^{-1}
Kinetic rate constant (positive)	1×10^{-11} m s^{-1}
Anodic and cathodic transfer coefficients in the positive and negative electrodes	0.5
Geometric cross-sectional area of the cell	0.0108 m^2
Thickness of graphite (negative porous insertion electrode)	59.1 μm
Solid phase lithium diffusivity in negative particle	2×10^{-14} m^2 s^{-1}
Solid phase lithium diffusivity in positive particle	7.49×10^{-13} m^2 s^{-1}
Thickness of the separator	21 μm
Thickness of $Li_y(Ni_aCo_bMn_c)O_2$ (positive porous insertion electrode)	50 μm
Separator porosity	0.48
Bruggeman exponent in separator	3

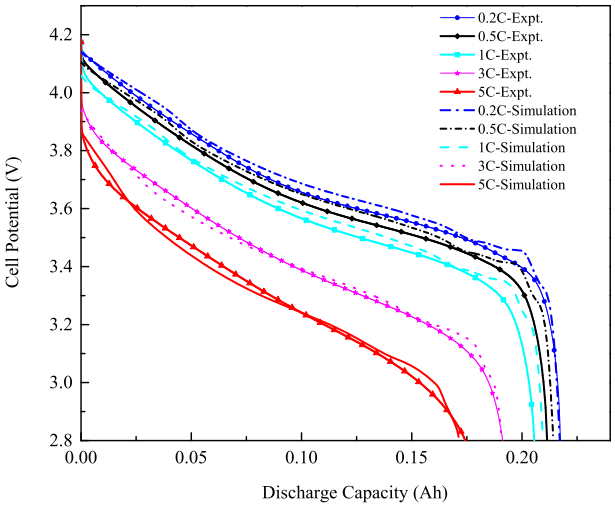

Fig. 1. Comparison between model predictions and experimental cell potential vs. capacity at various galvanostatic discharge rates.

However the cell overpotential mostly increases during 5C and 3C discharge. Fig. 3(a) and (b) shows the relative contributions from various phenomena in different regions to the cell overpotential during galvanostatic discharge at 5C and 3C rates respectively as a function of cell capacity from simulations. The solid black curves are from Fig. 2. The cell overpotential at 5C is 825 mV and at 3C is 440 mV. The various contributions that are discussed next during galvanostatic discharge at 5C and 3C are stacked in the respective plots in Fig. 3. The contributions add up to the total cell overpotential (black curve) quite well for 3C rate and up to 80 mAh for 5C rate and then a slight discrepancy is observed. The reason for this discrepancy could be that the charge transfer overpotential shown in Fig. 3 is obtained by taking average across the respective regions and not measured just at terminals. Fig. 3(a) shows that at a 5C rate, at the very beginning of discharge, the charge transfer overpotentials at the electrodes dominate the cell overpotential. But as time progresses, salt concentration overpotential in the positive electrode significantly increases and is accompanied by an increase in the ionic ohmic drop as well. Fig. 3(b) shows that at a 3C discharge rate, although the salt concentration overpotential increases as discharge proceeds, the charge transfer overpotentials in the electrodes dominate the cell overpotential.

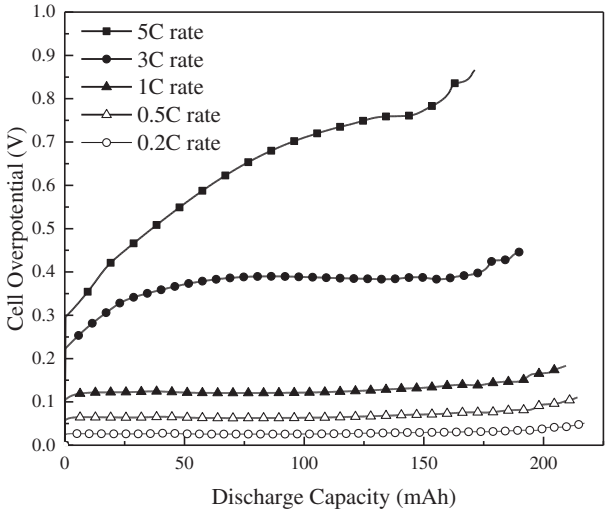

Fig. 2. Cell overpotential vs. discharge capacity from simulations.

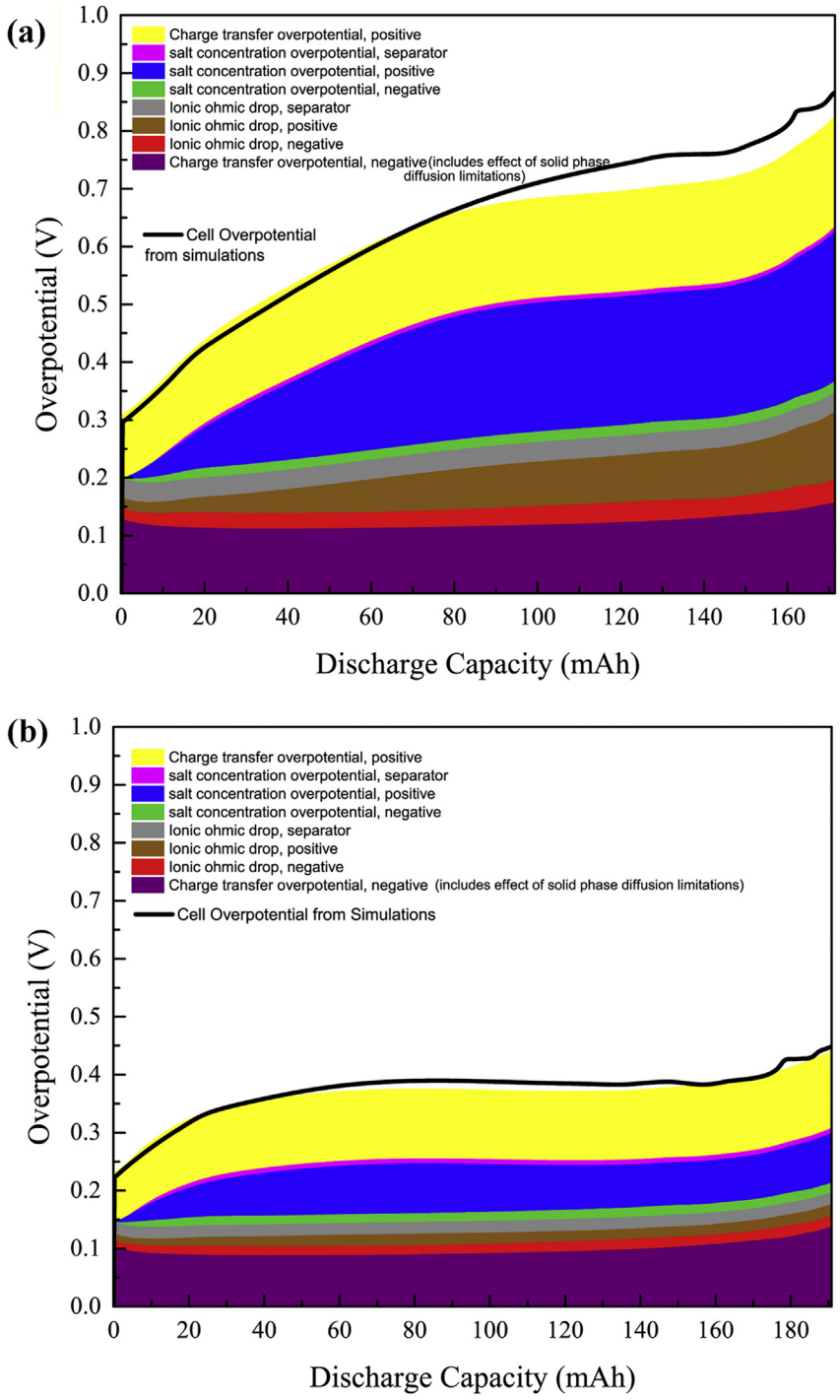

Fig. 3. (a) Overpotential vs. discharge capacity at 5C rate. (b) Overpotential vs. discharge capacity at 3C rate.

In the simulated plots that are discussed below symbols are provided for clarity and do not represent actual experimental data or are not the only simulated data points. The numeric values in the legend in the simulated plots represent the time since the beginning of discharge in seconds.

3.1.1. Matrix phase ohmic overpotential from electronic resistance of the composite electrode

The ohmic drop due to electronic resistances in the composite electrodes is negligible even at high rate such as 5C and the solid phase potential across each composite electrode is constant (hence figure not given) at any given time during discharge. Therefore the matrix phase ohmic overpotential from electronic resistances is not seen in Fig. 3.

3.1.2. Ionic resistance and the ohmic drop in the electrolyte phase

Salt concentration varies with time and position in the cell sandwich during discharge as shown in Fig. 4 at 5C (106.5 A m^{-2}). The salt is depleted at the back of the positive electrode (current collector/positive electrode interface) at 150 s. So the ionic

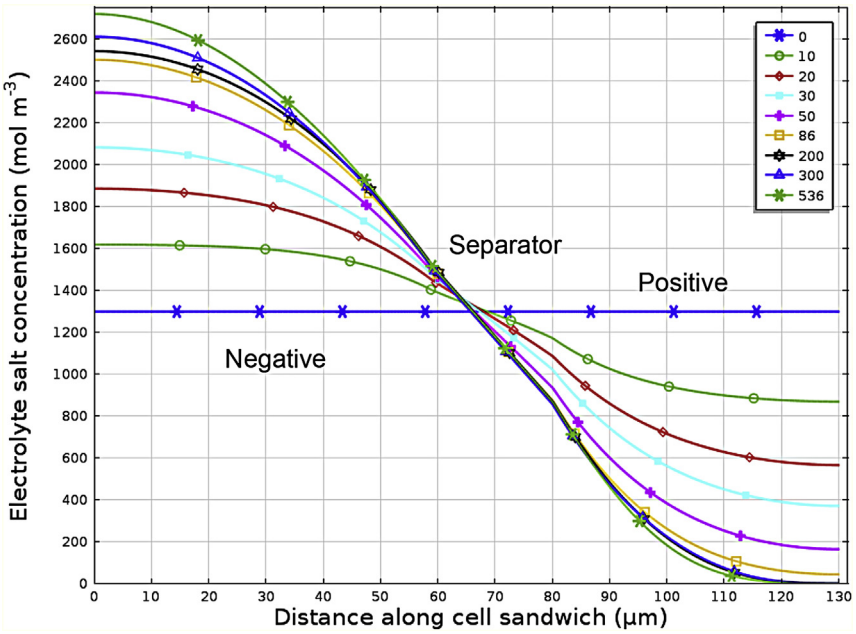

Fig. 4. Electrolyte concentration profiles across the cell sandwich at various times during galvanostatic discharge at 106.5 A m^{-2} (5C rate). Legend is discharge time in seconds.

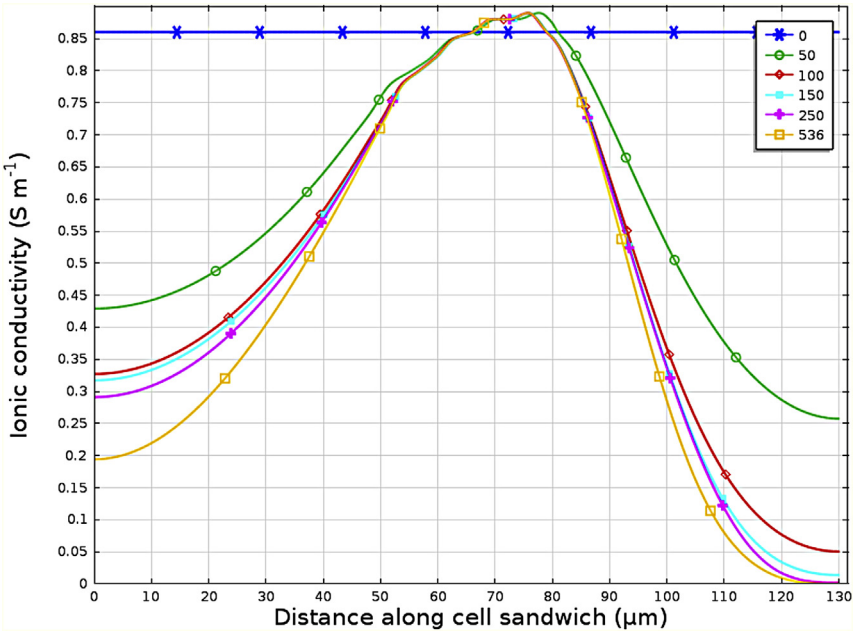

Fig. 5. Variation of ionic conductivity with time and position during 5C galvanostatic discharge. Legend is discharge time in seconds.

conductivity reaches zero there (Fig. 5) because ionic conductivity is a function of salt concentration (Fig. A-1). Therefore, as seen in Fig. 3(a), the ionic resistance in the electrolyte phase increases significantly in the positive electrode. As seen explicitly in Fig. A-2, the total ohmic drop at the end of discharge is 190 mV.

Salt depletion does not occur at 3C or lower discharge rates and therefore the ionic conductivity does not drop to zero. Therefore the ohmic drop in the electrolyte phase in the positive electrode is only 20 mV at 3C rate (Fig. 3(b) or Fig. A-3). The total ohmic drop in the electrolyte phase is 60 mV. If the void volume fraction in the positive electrode is increased to 0.33, it improves the effective liquid phase transport properties and then even at 5C discharge rate, salt depletion does not occur before the cut-off potential is reached at 539 s.[1] In this case, the ohmic drop due to ionic resistance in the positive is 30 mV. If the positive electrode void volume fraction is 0.29 (Table 1) and the bulk salt diffusivity is higher (than the value adjusted in this work to fit to experimental data) or enhanced with additives, we can once again expect performance improvements.

3.1.3. Total electrolyte phase potential drop

The overpotential due to ionic resistance and the salt concentration overpotential from all three regions of the cell contribute to

[1] The discharge capacity is almost the same as before due to similar discharge times.

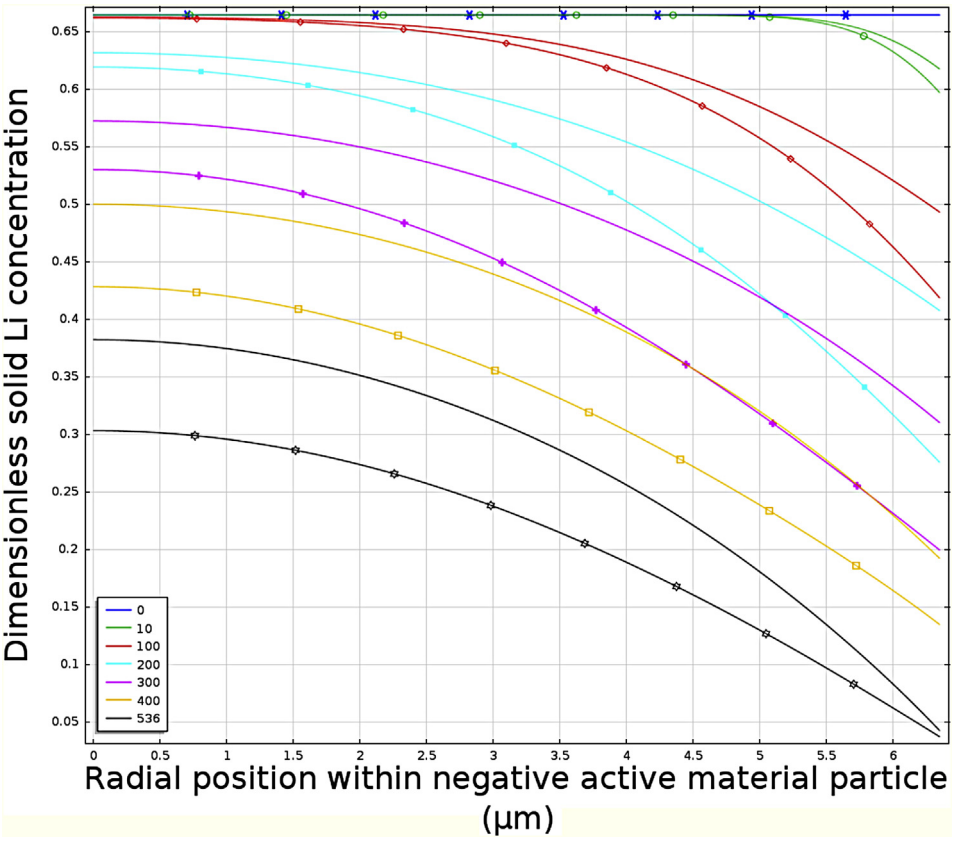

Fig. 6. Radial solid Li profile within secondary negative active material particle at 5C discharge rate. Curves with (a) markers: at electrode/separator boundary; (b) no markers: at current collector/electrode boundary. Legend is discharge time in seconds.

the total electrolyte phase potential drop. The electrolyte phase potential drop across the whole cell at 5C discharge rate can be calculated from Fig. 3(a) and is provided in Fig. A-2. Towards the end of discharge, the liquid phase potential drop has increased to 475 mV because of significant ohmic drop and salt concentration overpotential. Corresponding data at 3C rate is provided in Fig. A-3 and the total electrolyte phase overpotential is 170 mV. The mass transport limitations in the electrolyte and the corresponding salt concentration overpotential mentioned above are discussed in detail later in this paper.

3.1.4. Charge transfer overpotential

The Butler Volmer form of expression [8] is used in the simulations to describe the charge transfer kinetics. The charge transfer overpotentials obtained from detailed simulations seen in the stacked plot in Fig. 3 are also shown in Figs. A-4 and A-5 for discharge at 5C and 3C respectively for clarity. Charge transfer overpotential could have been influenced by solid phase diffusion limitations, as discussed later. Film resistance, although not considered explicitly in this work, is a possible contribution to the charge transfer overpotential.

3.1.5. Mass transport limitations and concentration overpotential in the electrolyte phase

The concentration overpotential in the electrolyte phase depends on salt concentration and its gradient in the cell which is affected by different transport properties such as the less-than-unity transference number, the bulk salt diffusion coefficient and the thermodynamic factor that accounts for a non-ideal electrolyte as well as the porosity and tortuosity. Concentration overpotential in the electrolyte phase from the simulation results at 5C discharge rate in each region of the cell can be seen in Fig. 3(a) and is obtained by stacking the various contributions from Fig. A-2. The significant increase in overpotential at the positive (260 mV) is due to the salt depletion at the back of the electrode as the salt concentration is related to liquid phase potential drop through modified Ohm's law. Salt concentration overpotential increases during discharge at 3C rate too in the positive because of decreasing concentration. It is 110 mV towards the end of discharge (Fig. A-3). If the void volume fraction in the positive electrode is higher, say, 0.33, salt depletion does not occur at 5C rate by the time cut-off potential is reached at 539 s and the salt concentration overpotential in the positive is only 100 mV in the positive electrode region. Furthermore, because salt concentration appears in the expression for exchange current density, surface overpotential decreases by 10–15 mV for higher porosity.

3.1.6. Solid phase diffusion limitations and an estimate of 'solid concentration overpotential'

The time constants for lithium diffusion in the solid phase (spherical, secondary active material particle) are 2016 s in the negative and 35 s in the positive electrodes whereas the ideal discharge time at 5C rate is 720 s and at 3C rate is 1200 s. Therefore solid phase diffusion limitations exist in the negative and is negligible in the positive at both 5C and 3C constant current densities. Inter-particle diffusion, i.e. solid phase diffusion of lithium between particles in the electrode thickness direction is not considered. Fig. 6 gives the solid lithium concentration within the secondary particles of negative electrode as a function of radial position at two different locations along the electrode thicknesses, namely, separator/electrode boundary and the current collector/electrode boundary at 5C discharge. Irrespective of the location along the thickness of the negative composite electrode, as expected, there is a variation of Li

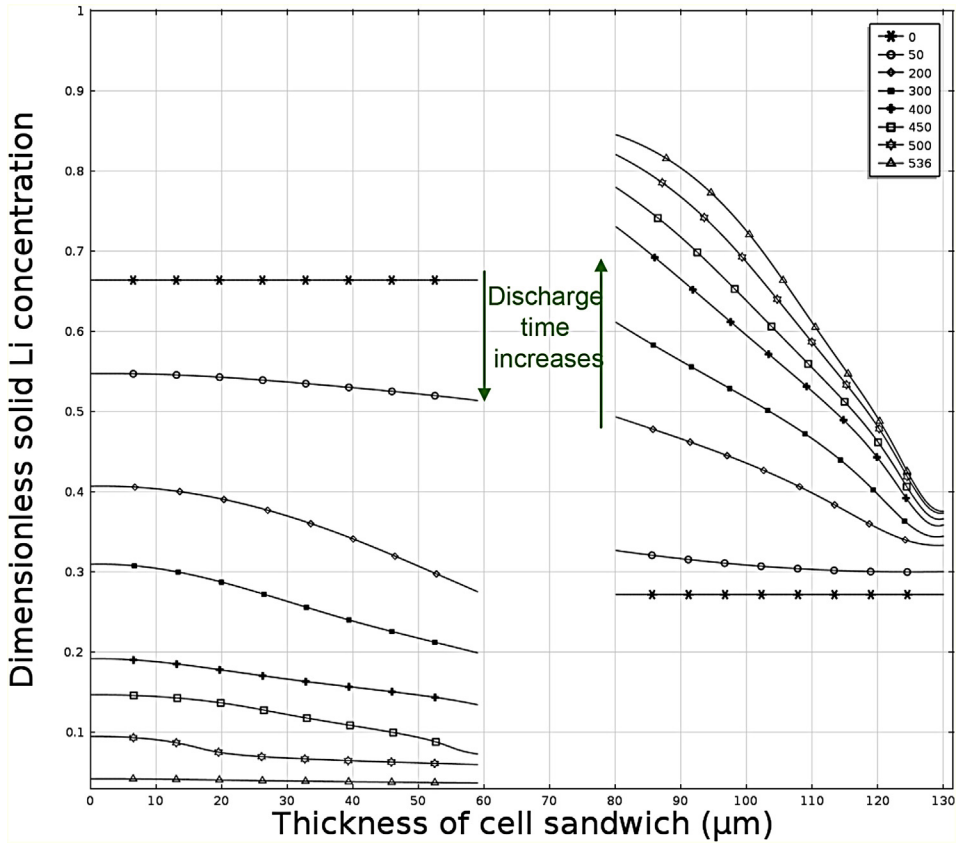

Fig. 7. Dimensionless solid lithium concentration profile at the surface of the active material particle across cell sandwich during discharging at 5C. Legend is discharge time in seconds.

concentration between the center and surface of the negative active material particle, thus verifying the quick estimates.

Solid phase diffusion limitations within the secondary, spherical active material particle also influence the lithium concentration at the surface of the particle across the cell sandwich (Fig. 7) and therefore the performance in two ways: (a) The solid lithium concentration at the surface of the secondary particle influences the exchange current density for the charge transfer reaction at the electrode/electrolyte interface (which in turn can affect the charge transfer overpotential). (b) The thermodynamic open-circuit potential (OCP) at any location within the electrode is evaluated using the concentration of lithium at the surface of the particle at that location. The OCP appears in the current–overpotential relationship and thus again influences the charge transfer overpotential. For these reasons, even though there is no concentration overpotential in the solid phase that is added directly to obtain the cell overpotential, the solid phase diffusion limitations are reflected in the cell overpotential.

To semi-quantitatively get an idea of the influence of solid phase diffusion limitations in the negative electrode on cell performance, the solid phase diffusion coefficient of Li in the negative active material particle is artificially increased by an order of magnitude. The cell discharge capacity obtained before reaching the cut-off potential is 190 mAh or an increase of 9% in terms of SOC from the 171 mAh obtained before at 5C rate. The average charge transfer overpotential in the negative is only 140 mV at the end of discharge (compared to 155 mV in Fig. 3(a) or Fig. A-4). Since salt depletion occurs in the positive and this zone moves from the back of the electrode towards the separator/positive electrode interface for a longer discharge time than in Fig. 4, the salt concentration overpotential in the positive is 380 mV at the end of discharge (compared to 260 mV in Fig. 3(a)), leading to a higher cell overpotential than before. At 3C discharge rate, the cell capacity again increases by 9% SOC for an order of magnitude increase in the solid phase diffusivity of Li in the negative. But the charge transfer overpotential remains the same at the end of discharge while liquid phase potential drop and therefore the total cell overpotential increases.

In Fig. 7, closer to the separator/positive electrode interface, the solid Li concentration attains 88% of the theoretical maximum solid lithium concentration (as restricted in the model development section) towards the end of the discharge at 5C rate. However, closer to the current collector/positive electrode interface, it shows only small variation from its initial value even at the surface of the particle. These suggest that non-uniform reaction rate distribution exists along the thickness of the positive electrode and will be examined next.

3.1.7. Current density distributions and local utilization across the cell sandwich

The reaction rate (current density) distributions across the composite electrodes in the cell during galvanostatic discharge at 5C rate are presented in Fig. 8. The corresponding local utilization of the active material (the average of the dimensionless solid Li concentrations at the surface and center of the particle) is plotted across each electrode in the cell sandwich direction in Fig. 9 and this allows one to examine the relationship between utilization and the thickness of the composite electrode. It should be noted that due to lack of solid phase diffusion limitations in the positive electrode particle, the utilization in Fig. 9 and surface Li concentration (Fig. 7) are almost the same across the positive electrode. The current distribution is highly non-uniform and complex in the positive electrode. At 5C discharge rate, even at short times, due to low salt concentrations, the effect of mass transport limitations in

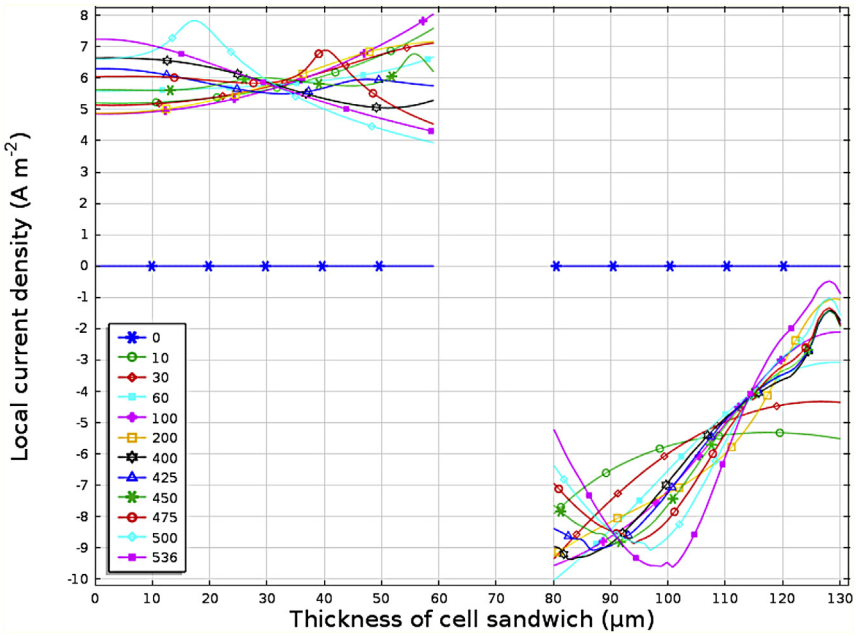

Fig. 8. Local current density at the electrode/electrolyte interface while discharging at 5C rate. Legend is discharge time in seconds.

the electrolyte phase comes into effect and as can be seen from Fig. A-2, the total liquid phase potential drop reaches 100–110 mV. As discharge proceeds, salt depletion at the back of the positive electrode not only causes significant concentration overpotential, but also affects charge transport and the kinetic expression (limiting current phenomenon is reached at this boundary). When the reaction front is skewed towards the front of the positive electrode/separator interface, the surface Li concentration relatively increases at this boundary compared to at the back (positive electrode/current collector interface). However, as discharge proceeds and the maximum allowed solid Li concentration is approached on the surface of the positive active material particle (Fig. 7 or local utilization from Fig. 9, because of facile solid phase diffusion) at the front of the electrode, the reaction front slightly shifts inwards (i.e. away from separator/electrode interface) in the positive region. It is apparent from Fig. 9 that the material near the back face of the positive electrode is not fully utilized at 5C discharge rate. At 3C discharge rate, due to lack of solid phase

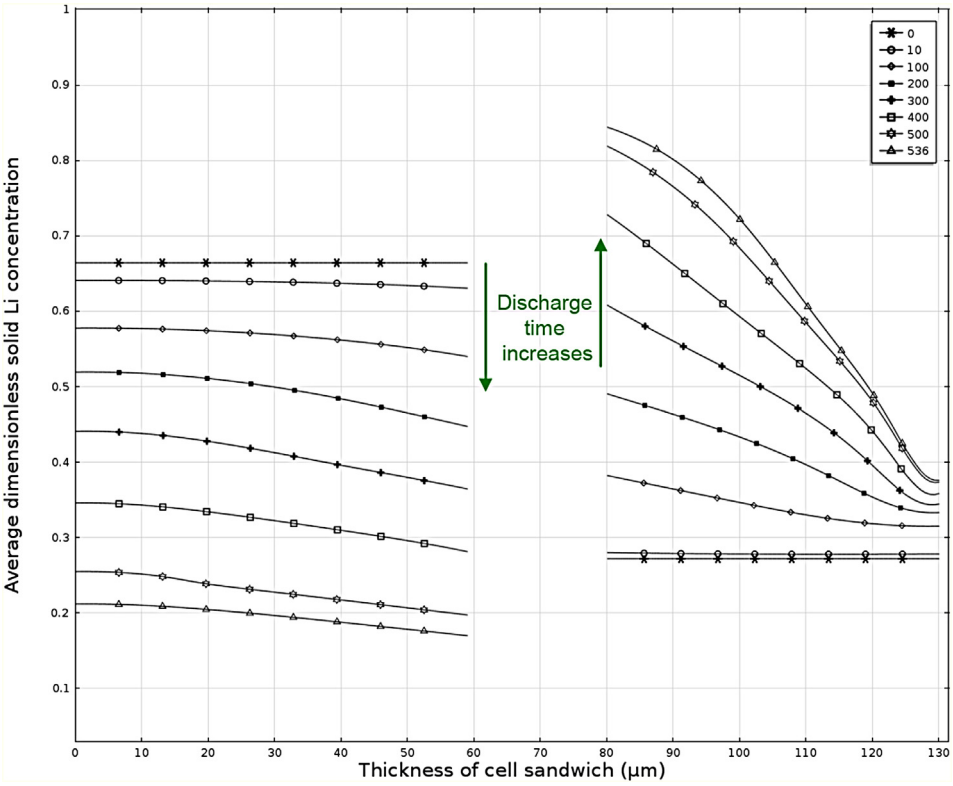

Fig. 9. Local utilization of active material across the full cell during discharge at 5C rate. Legend is discharge time in seconds.

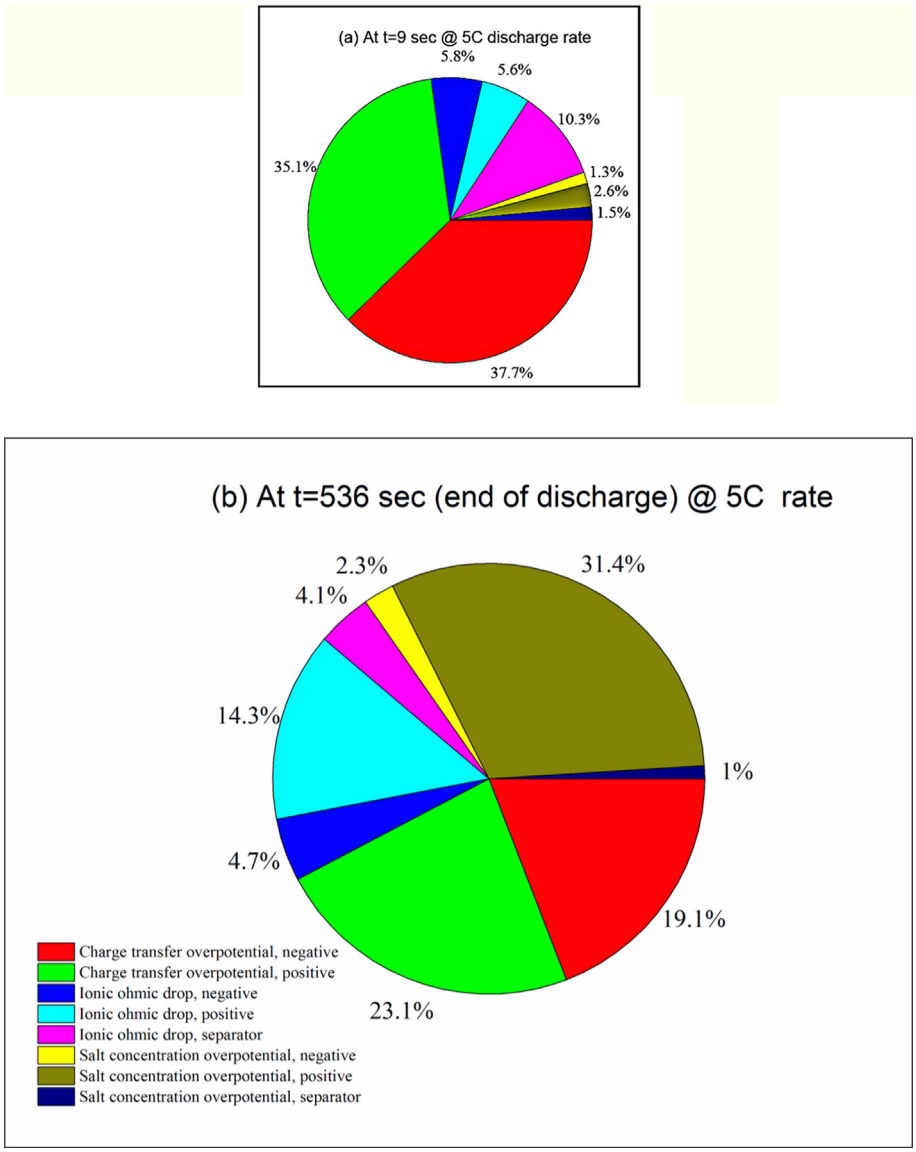

Fig. 10. Contributions to the cell overpotential during 5C rate of galvanostatic discharge at (a) 9 s since the beginning of discharge and (b) the end of discharge.

diffusion limitations in the positive, Fig. A-6 can be considered to indicate local utilization and give insight into reaction current distribution across the composite electrode. Because of the dominant effect of charge transfer overpotential at 3C rate as seen in Fig. 3(b) (in both the electrodes), the Li profile in Fig. A-6 is relatively uniform as compared to that at a 5C discharge rate (Fig. 9).

The reaction rate distribution across the negative electrode is relatively uniform at 5C discharge rate (Fig. 8) and the local current density varies only between 4 and 8 A m^{-2}. Surface overpotential dominates the limitations in the negative electrode (Fig. 3(a)). At long times (~450–505 s), even though the active material is not completely utilized at the front of the negative electrode (boundary with the separator), the reaction front moves as a small spike towards the back (current collector/electrode interface). Except for a slight inflection in the exchange current density profile (corresponding to the surface Li concentration profile in Fig. 7 in the negative electrode), no local maxima or minima are observed in the exchange current density profile that can explain the spikes in local current density. However, it is found that the spatio-temporal progression of the spikes in the reaction current distribution correspond to that of the local minima in thermodynamic OCP at low surface solid Li concentration that is reached during discharge of the full cell at long times in the negative.

3.2. Summary of relative contributions to total cell overpotential

The contributions (in percentages) of the various processes from different regions of the cell at two different times (i.e. 9 s and at the end of discharge) from Fig. 3 at 5C discharge rate to the total cell overpotential at the corresponding times are shown in respective pie charts in Fig. 10. Fig. 11 provides these contributions for 3C discharge rate. The pie charts are approximately sized to the ratio of the cell overpotentials at the corresponding times at each rate (there is no correlation/scaling of the size of the pie charts between rates). Figs. 3(a) and 10 shows that at 9 s into discharge, the salt concentration overpotential contributed to 2.6% of 328 mV which is the cell overpotential at that time. However, at the end of discharge at 536 s, the contribution from the salt concentration overpotential has increased to 31.4% of the cell overpotential of 824 mV and has become the dominant factor. The contribution from ohmic drop due to ionic resistance has increased to 14.3% at the end of discharge. Similarly, during 3C

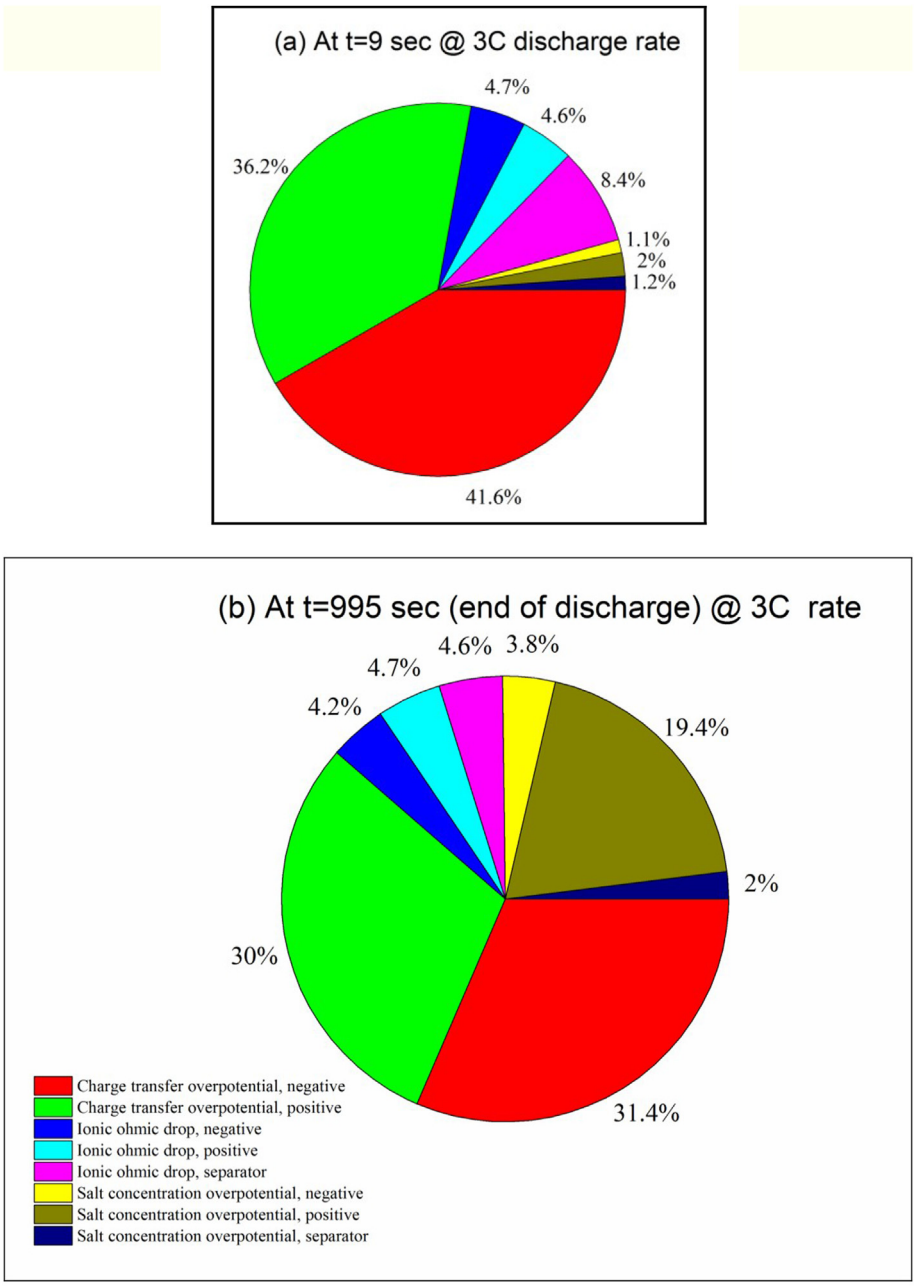

Fig. 11. Contributions to the cell overpotential during 3C rate of galvanostatic discharge at (a) 9 s since the beginning of discharge and (b) the end of discharge.

discharge, at 9 s, the salt concentration overpotential is 4.82 mV whereas at the end of discharge at 995 s, it has increased to 85.4 mV. However, the charge transfer overpotentials in both the electrodes continue to be the dominating factor during discharge at 3C rate. This contribution, as noted earlier is also influenced by solid phase diffusion limitations in the negative.

4. Conclusions

The simulation results from an isothermal physics-based dual lithium-ion insertion cell sandwich model are validated with experimental data at various constant-current discharge rates. The cell overpotential is higher at higher discharge current density. Also, at a given rate, as discharge proceeds, the cell overpotential increases and the relative contributions of different processes vary. The various contributions to the cell overpotential are quantified and analyzed in detail at both 3C and 5C galvanostatic discharge rates. Depending on the application, i.e. HEV or PHEV or EV, the state of charge (SOC) window of operation and the current pulse magnitudes that the cell experiences can vary [9] and therefore accordingly, the appropriate limitations as identified in this work have to be addressed. Furthermore, the overpotential losses will vary with alternate chemistries such as silicon negative electrode [10,11] or solid electrolytes. However, the framework discussed in this work can be used to analyze overpotential losses in other lithium-ion cell chemistries as well. Calculations in this work are based on the cell sandwich model and therefore while extending these analyses to large format cells, non-uniform current distributions across the cell geometries have to be considered. This work provides insight and methodology for materials research and development, cell design and battery

controls to avert or circumvent these limitations and enable the use of lithium-ion cells in advanced electric vehicles.

Acknowledgments

Andy Drews and Ted Miller are acknowledged for their support. The experimental data were provided by the Samsung SDI team for the prior work [6].

Appendix A

The bulk ionic conductivity of the electrolyte ($LiPF_6$ in EC:EMC:DMC in the ratio 3:4:3), measured by electrolyte suppliers in the presence of additives, is provided in Fig. A-1. The measurements were not possible beyond 3 M because the salt did not dissolve in the solvent.

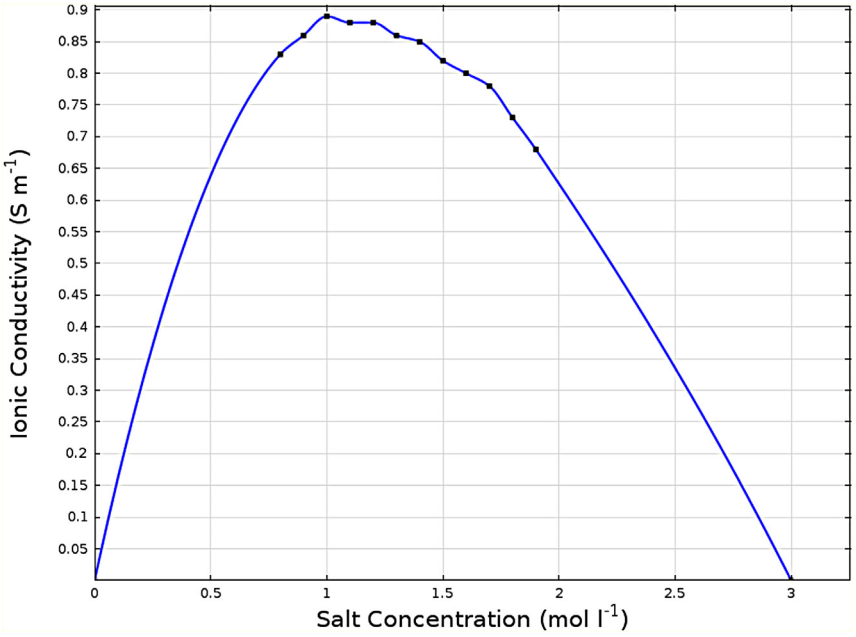

Fig. A-1. Ionic conductivity of $LiPF_6$ in EC:EMC:DMC (3:4:3, with additives) at room temperature from experiments (symbols represent actual data points).

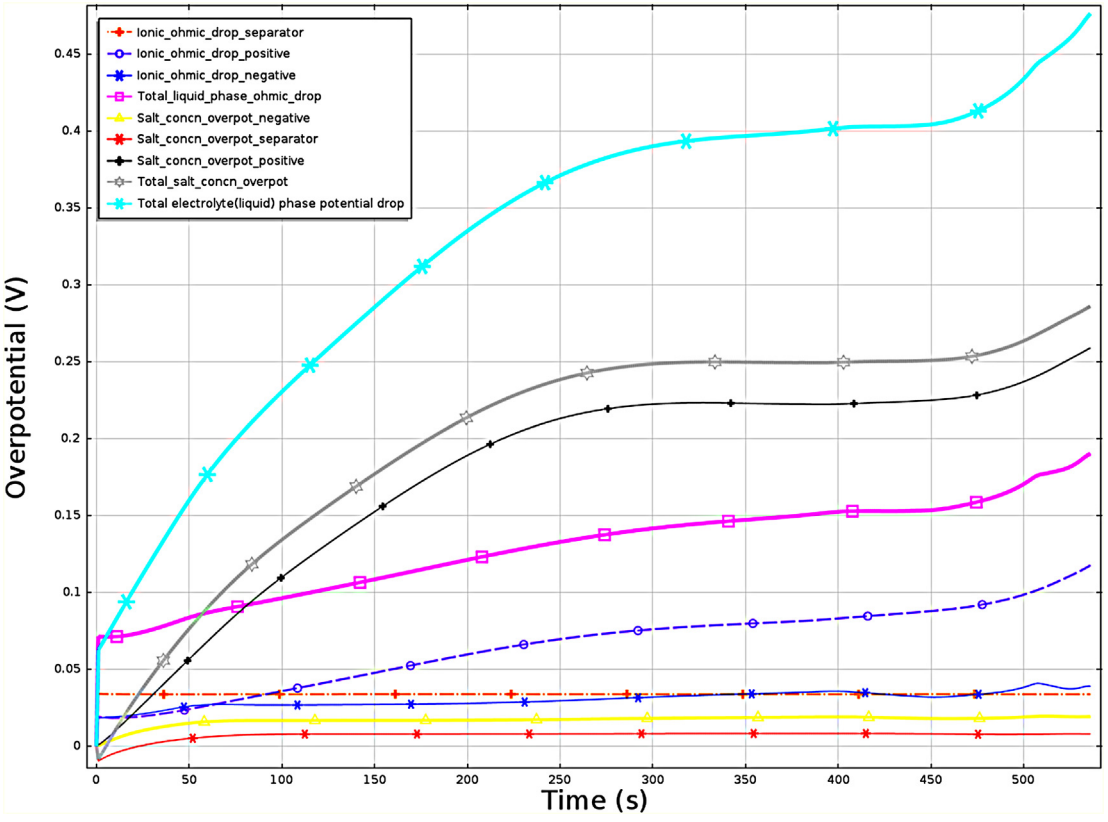

Fig. A-2. Contributions to the potential drop in the electrolyte phase at 5C discharge rate as a function of time (Ref: Li/Li^+).

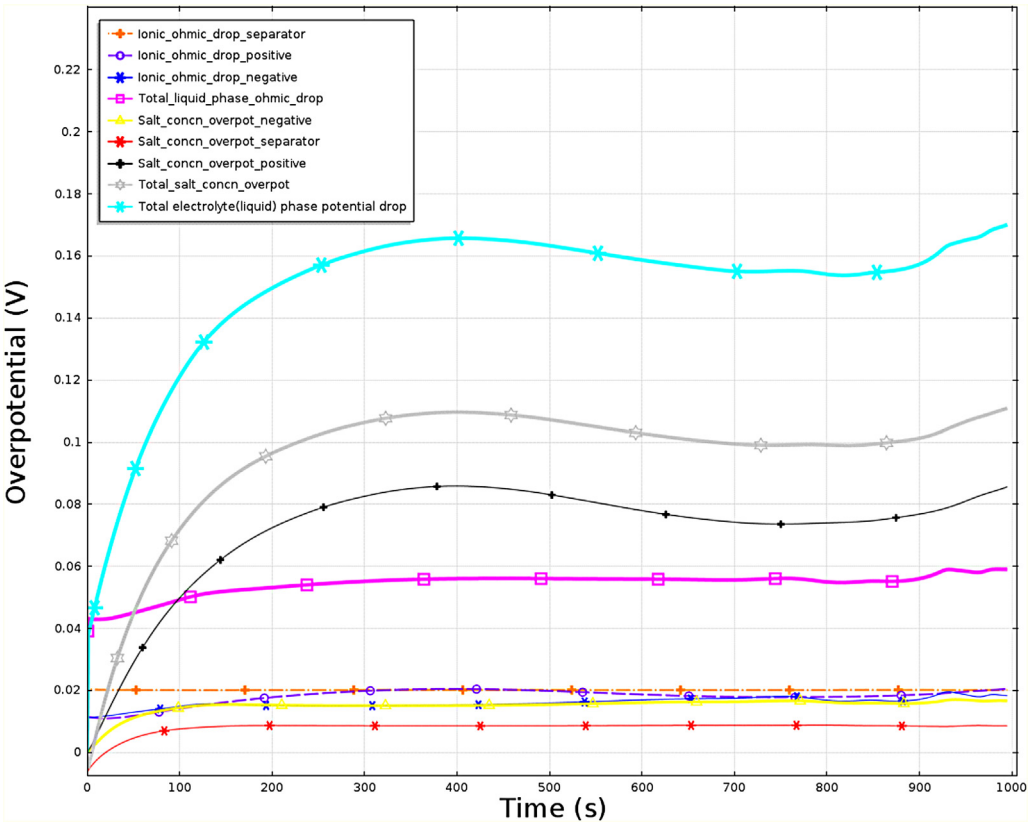

Fig. A-3. Liquid electrolyte phase potential drop during 3C discharge rate.

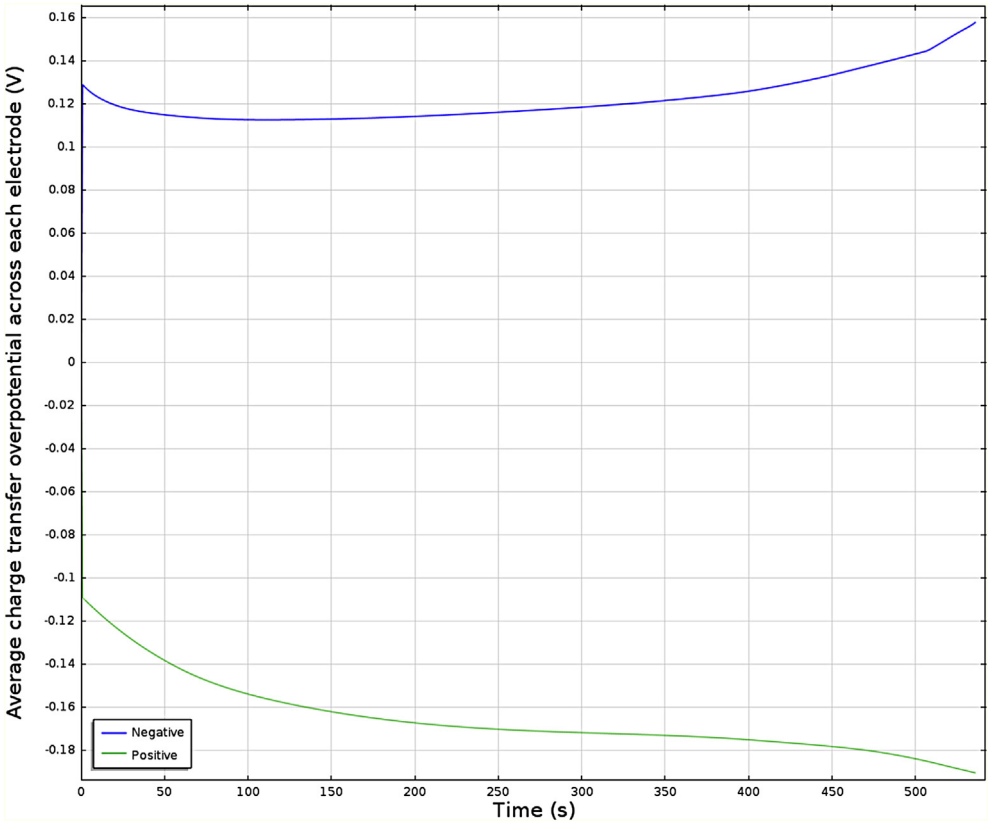

Fig. A-4. Average charge transfer overpotential in each composite electrode while discharging at 5C rate as a function of time (Li/Li^+ Ref.).

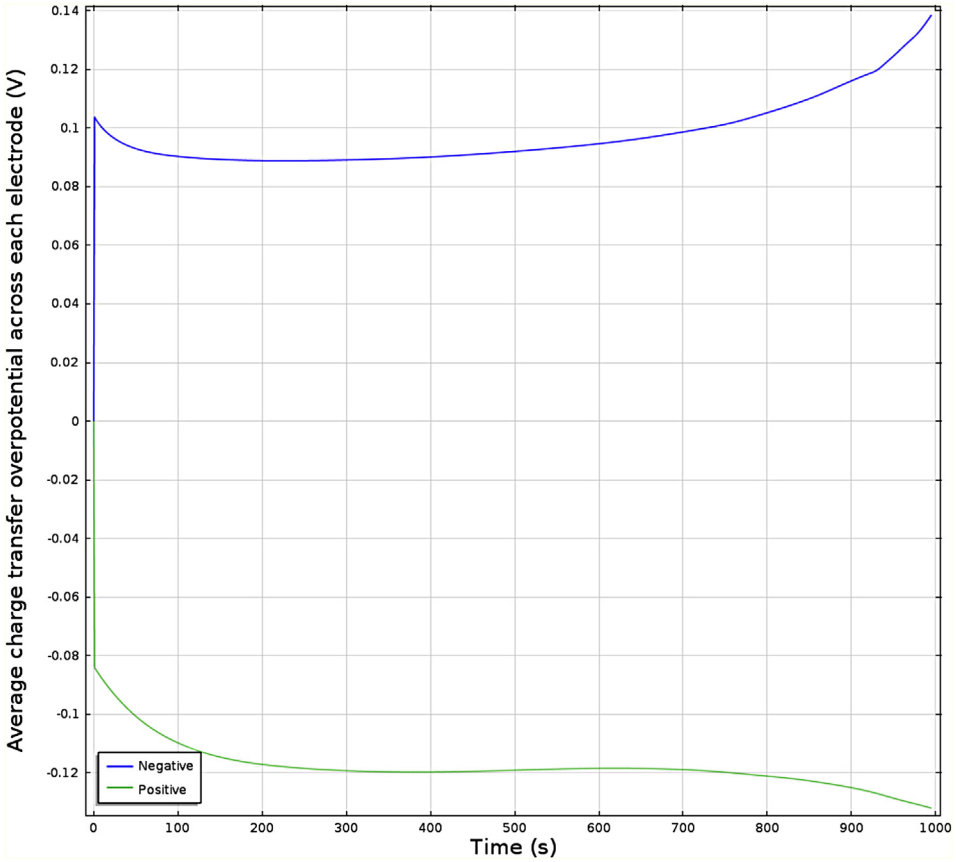

Fig. A-5. Average charge transfer overpotential during galvanostatic discharge at 3C rate.

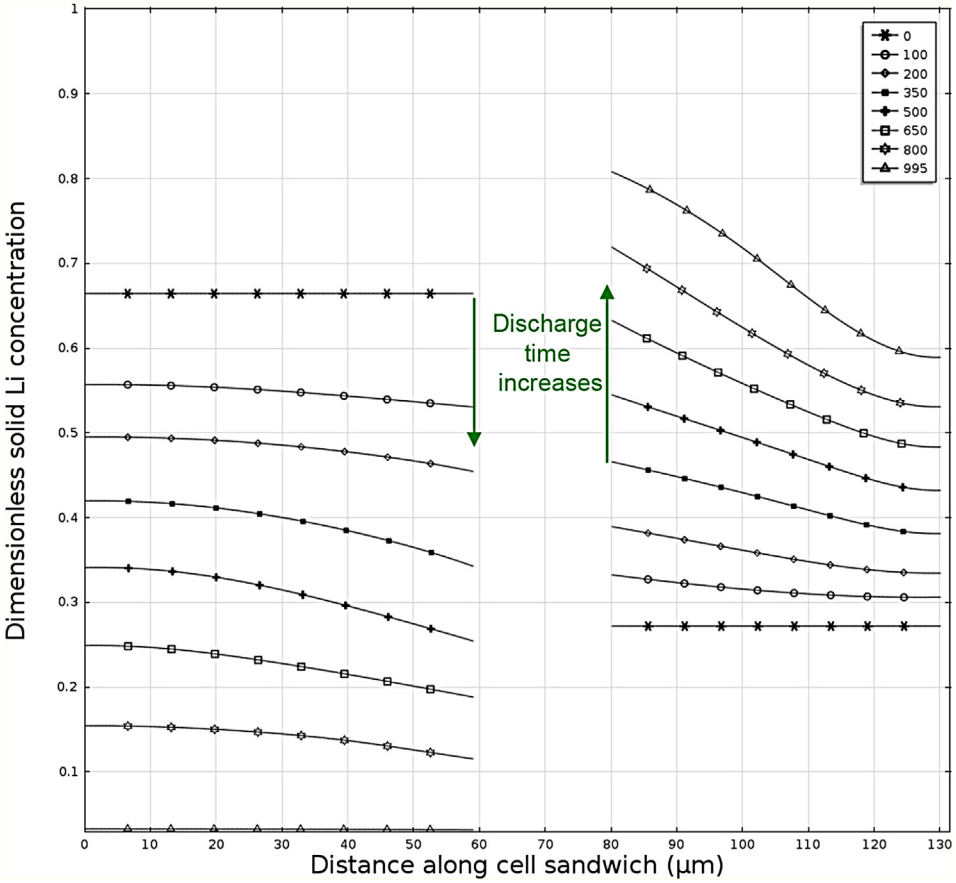

Fig. A-6. Dimensionless solid lithium concentration profile at the surface of the active material particle across cell sandwich during discharging at 3C. Legend is discharge time in seconds.

References

[1] G. Sikha, B.N. Popov, R.E. White, J. Electrochem. Soc. 151 (2004) A1104–A1114.
[2] P. Ramadass, B. Haran, R.E. White, B.N. Popov, J. Power Sources 112 (2002) 614–620.
[3] R. Chandrasekaran, G. Sikha, B.N. Popov, J. Appl. Electrochem. 35 (2005) 1005–1013.
[4] D. Danilov, R.A.H. Niessen, P.H.L. Notten, J. Electrochem. Soc. 158 (2011) A215–A222.
[5] Y. Ji, Y. Zhang, C.-Y. Wang, J. Electrochem. Soc. 160 (2013) A636–A649.
[6] R. Chandrasekaran, Y. Seong, C. Bae, J. Jung, K. Kim, K. Cheong, T.J. Miller, Materials Research Society Online Proceedings Library, MRSS13-1541-F04-05, 2013.
[7] M. Doyle, T.F. Fuller, J.S. Newman, J. Electrochem. Soc. 140 (1993) 1526–1533.
[8] T.F. Fuller, M. Doyle, J.S. Newman, J. Electrochem. Soc. 141 (1994) 1–10.
[9] R. Chandrasekaran, W. Bi, T.F. Fuller, J. Power Sources 182 (2008) 546–557.
[10] R. Chandrasekaran, A. Magasinski, G. Yushin, T.F. Fuller, J. Electrochem. Soc. 157 (2010) A1139–A1151.
[11] R. Chandrasekaran, T.F. Fuller, J. Electrochem. Soc. 158 (2011) A859–A871.